MULTEM image simulation software
Solution sheet

Dr. Ivan Lobato, Annelies De wael and Thomas Friedrich

{ivan.lobato, annelies.dewael, thomas.friedrich}@uantwerpen.be

Exercise 1 - Acceleration voltage

With decreasing acceleration voltage the energy decreases and the wavelength increases. This results in a broader probe at 80 kV (Figure 1a) as compared to 300 kV (Figure 1b). The broader profile and larger wavelength practically reduces the resolution in the (S)TEM image.

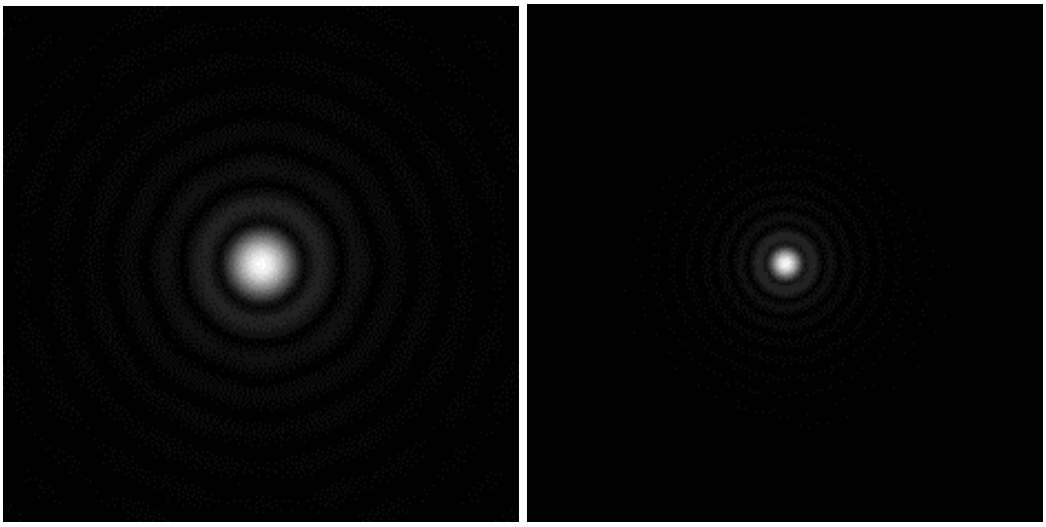

(a) 80 kV **(b)** 300 kV

Figure 1: Acceleration voltage

Exercise 2 - Aberrations

Aberrations are modeled by means of an aberration function χ. The transfer function of the objective lens is then $H_0(k) = e^{-i\chi(k)}$. The imaging wave function Ψ_i is a product of the transmitted wave function $\Psi_t(k)$ and $H_0(k)$. This means that in real space, the transfer function of the objective lens is convolved with the transmission wave function and therefore has decisive influence on the image formation $g(x)$.

$$g(x) = |\psi_i(x)|^2 = \left|FT^{-1}\left[\Psi_i(k)\right] \otimes FT^{-1}\left[H_0(k)\right]\right|^2, \tag{1}$$

where FT^{-1} denotes inverse Fourier transforms [Kirkland, 2010].

a) Defocus

The defocus Δf is rotationally symmetric and its influence on the aberration function $\chi(k)$ is shown in equation (2).

$$\chi(k) = \pi\lambda k^2 \left(0.5C_s\lambda^2k^2 \boxed{-\Delta f}\right), \tag{2}$$

where C_s is the spherical aberration, k is the spatial frequency in the image plane, λ is the wavelength and Δf the defocus.
Generally, smaller aberrations allow for a smaller probe and therefore, a better resolution. The optimal defocus value (Scherzer defocus) can be found using equation 3 [Kirkland, 2010]. This function is included in MULTEM and can be called by clicking the *Opt* button.

$$\begin{aligned} \Delta f &= \sqrt{(2n_D - 0.5)\, C_S \lambda} \\ n_D &= 1, 2, 3... \end{aligned} \tag{3}$$

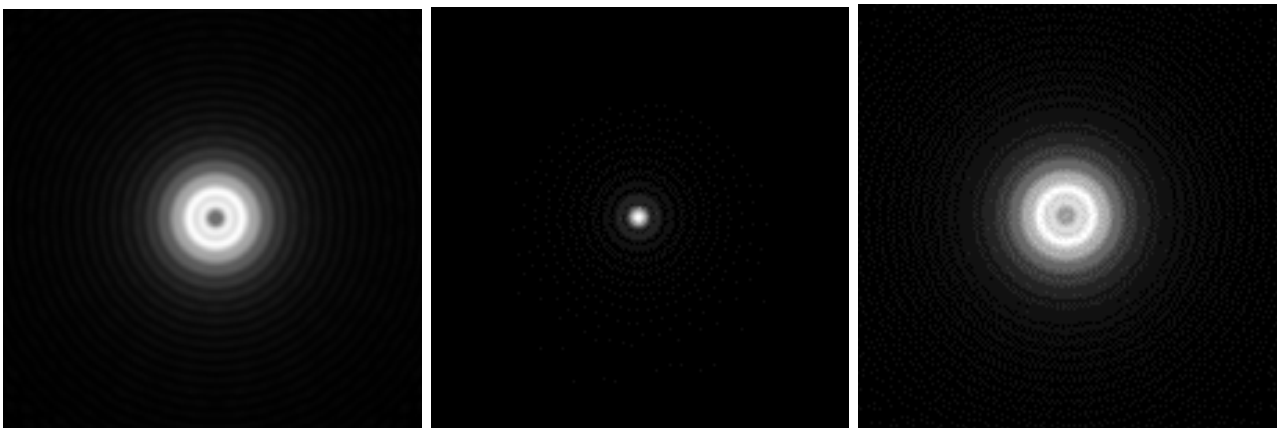

(a) $C_{10} = -100\,\text{Å}$ **(b)** $C_{10} = -14.031\,\text{Å}$ **(c)** $C_{10} = 100\,\text{Å}$

Figure 2: Spherical aberration

b) Spherical aberration

The spherical aberration C_s is also rotationally symmetric and its influence on the aberration function $\chi(k)$ is shown in equation (4).

$$\chi(k) = \pi\lambda k^2 \left(0.5\, C_s\, \lambda^2 k^2 - \Delta f\right), \tag{4}$$

The effect of spherical aberration can be compensated to some extent, by applying an appropriate defocus (Scherzer defocus) as calculated by equation 3.

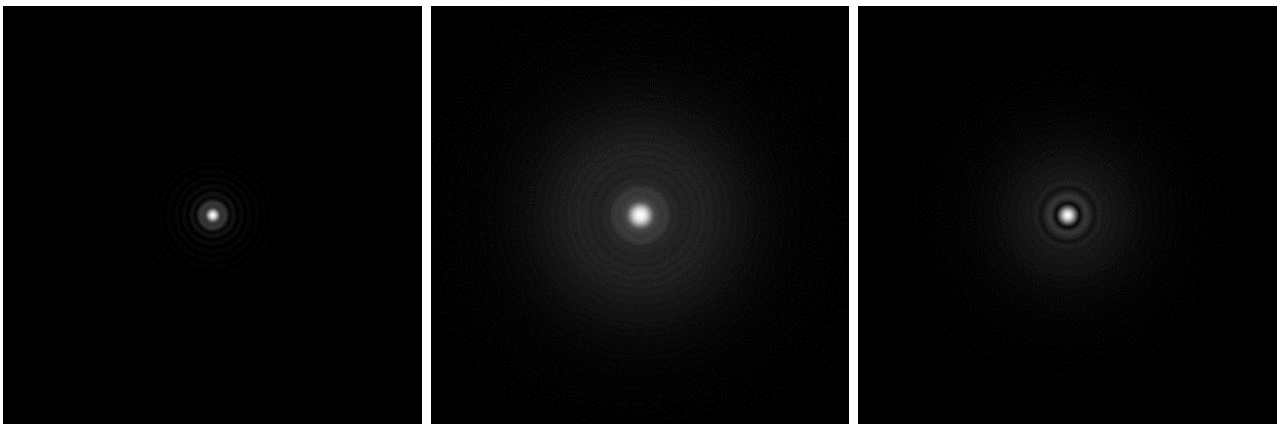

(a) $C_{30} = 0.01mm$
$C_{10} = -44.371\,\text{Å}$
(b) $C_{30} = 0.10mm$
$C_{10} = -44.371\,\text{Å}$
(c) $C_{30} = 0.10mm$
$C_{10} = -140.312\,\text{Å}$

Figure 3: Spherical aberration

c) Two-fold astigmatism

Equation (4) can be extended to include nonsymmetrical terms into the aberration function as shown in equation (5) [Kirkland, 2010]. The term describing the contribution of the two-fold astigmatism is highlighted.

$$\begin{aligned}\chi(k) =& \frac{\pi}{2} C_s \lambda^3 k^4 \\ & - \pi \Delta f \lambda k^2 \\ & \boxed{+\pi f_{a2} \lambda k^2 \sin\left[2(\phi - \phi_{a2})\right]} \\ & + \frac{2\pi}{3} f_{a3} \lambda^2 k^3 \sin\left[3(\phi - \phi_{a3})\right] \\ & + \frac{2\pi}{3} f_{c3} \lambda^2 k^3 \sin\left[\phi - \phi_{c3}\right]\end{aligned} \tag{5}$$

Ideally - without astigmatism - both the probe module and the phase should be radially symmetric. One can clearly see the influence of two-fold astigmatism on the probe module in Figure 4a and the phase in Figure 4b. Figures 4c and 4d show the same effect, but with an azimuthal angle of 45°

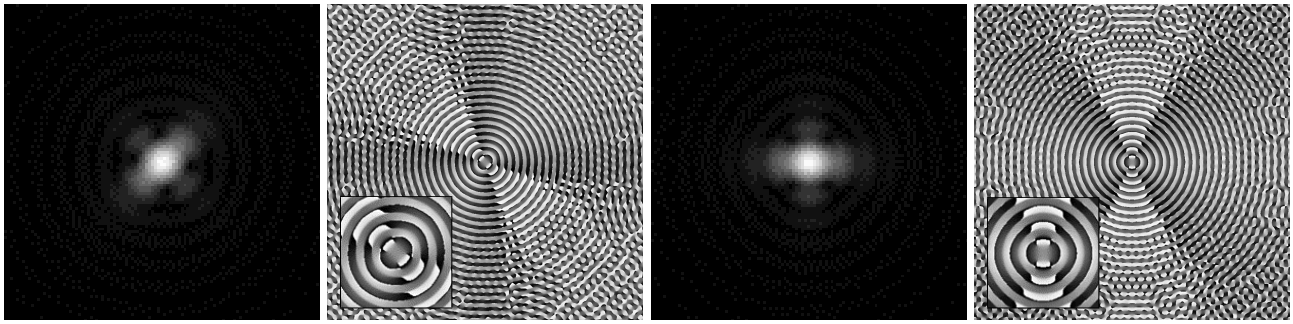

(a) Module $C_{12} = 20\,\text{Å}$ $\phi_{12} = 0°$ | **(b)** Phase $C_{12} = 20\,\text{Å}$ $\phi_{12} = 0°$ | **(c)** Module $C_{12} = 20\,\text{Å}$ $\phi_{12} = 45°$ | **(d)** Phase $C_{12} = 20\,\text{Å}$ $\phi_{12} = 45°$

Figure 4: Two-fold astigmatism

d) Three-fold astigmatism

$$\begin{aligned}\chi(k) =& \frac{\pi}{2} C_s \lambda^3 k^4 \\ & - \pi \Delta f \lambda k^2 \\ & + \pi f_{a2} \lambda k^2 \sin\left[2(\phi - \phi_{a2})\right] \\ & \boxed{+\frac{2\pi}{3} f_{a3} \lambda^2 k^3 \sin\left[3(\phi - \phi_{a3})\right]} \\ & + \frac{2\pi}{3} f_{c3} \lambda^2 k^3 \sin\left[\phi - \phi_{c3}\right]\end{aligned}$$

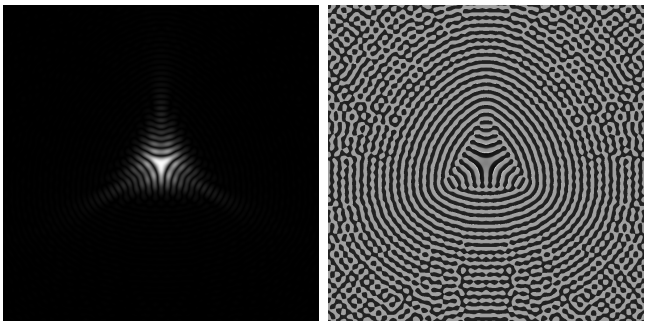

(a) Module | **(b)** Phase

Figure 5: Three-fold astigmatism, $C_{23} = 5000\,\text{Å}$

e) Coma

$$\begin{aligned}\chi(k) =& \frac{\pi}{2} C_s \lambda^3 k^4 \\ &- \pi \Delta f \lambda k^2 \\ &+ \pi f_{a2} \lambda k^2 \sin\left[2(\phi - \phi_{a2})\right] \\ &+ \frac{2\pi}{3} f_{a3} \lambda^2 k^3 \sin\left[3(\phi - \phi_{a3})\right] \\ &+ \frac{2\pi}{3} f_{c3} \lambda^2 k^3 \sin\left[\phi - \phi_{c3}\right]\end{aligned}$$

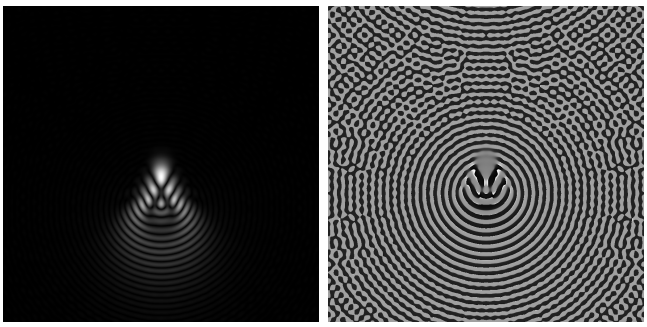

(a) Module **(b)** Phase

Figure 6: Coma, $C_{21} = 25\,000$ Å

Exercise 3 - Aperture outer radius

In principle, the largest possible outer aperture radius would be desirable, as the probe becomes smaller and smaller. However, a larger outer aperture radius also means that higher scattering angles contribute to the signal, which are influenced by aberrations a lot stronger. In practice, aberrations cannot be fully omitted or corrected, which means that increasing the outer aperture is always a trade off for an accentuation of aberration effects. Hence, the outer aperture radius cannot be chosen arbitrarily large, but is limited by the microscopes aberrations.

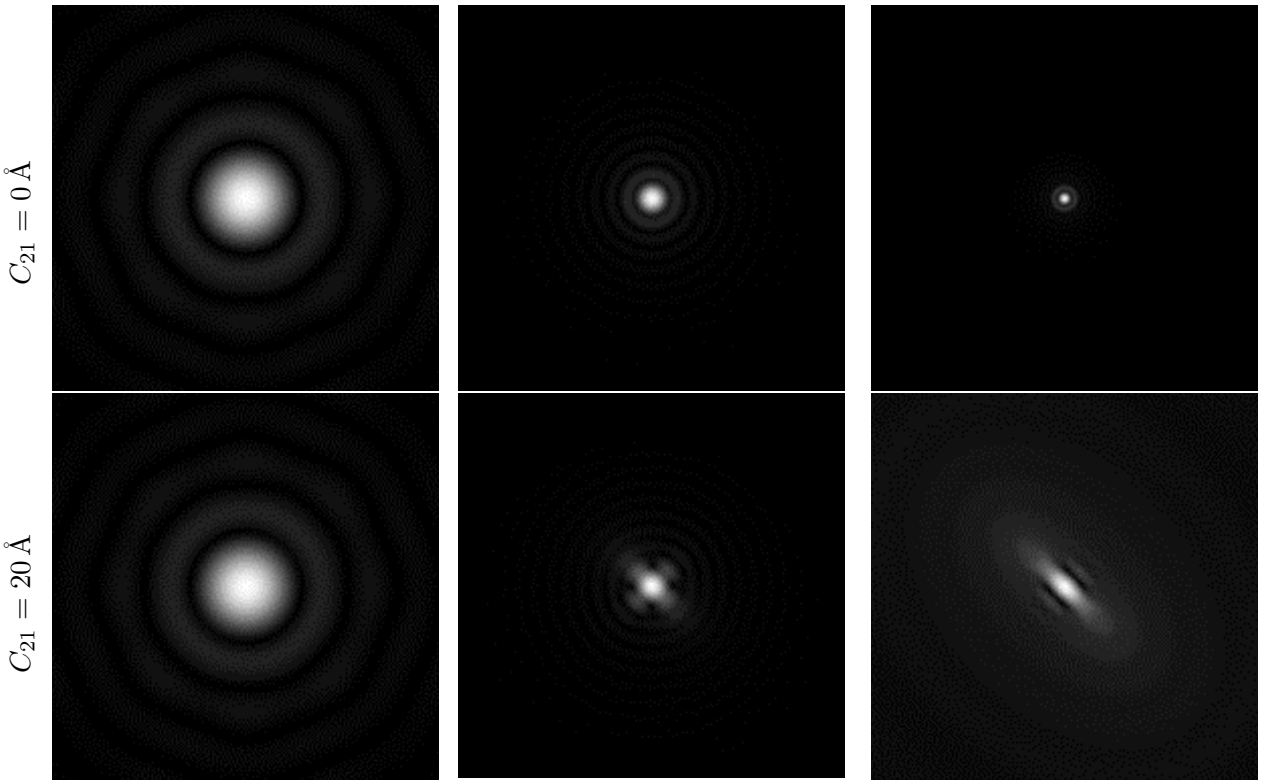

(a) 7 mrad **(b)** 21 mrad **(c)** 50 mrad

Figure 7: Aperture outer radius - The top row of images shows the probe a spherical aberration of $C_s = 0.001$mm and axial coma of $C_{21} = 0$ Å and the bottom row of images shows the probe with $C_s = 0.001$mm and $C_{21} = 20$ Å for each outer aperture radius.

Exercise 4 - Aperture inner radius

Blocking the central part of the electron beam by an inner aperture creates a so called Bessel beam, which changes phase according to a Bessel function. The biggest advantage of a Bessel beam is that it is very stable to defocussing. You could try and compare the probes for example for defocus values of -15, 0 and +15 for a normal probe and a Bessel beam. However, a large fraction of the intensity is lost using an inner aperture.

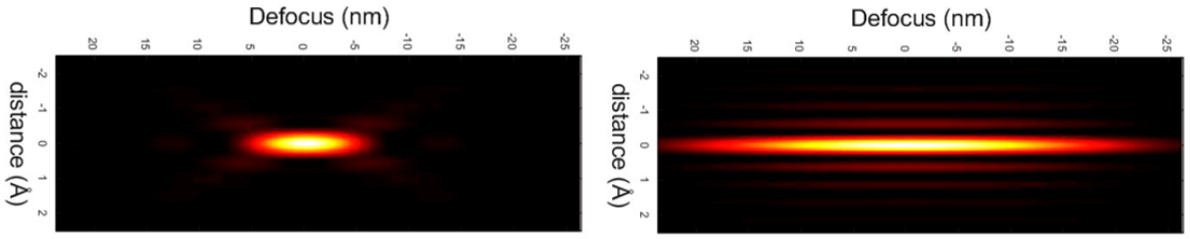

(a) Normal beam **(b)** Bessel beam

Figure 8: Comparison of normal and Bessel beam (Line profiles along defocus)

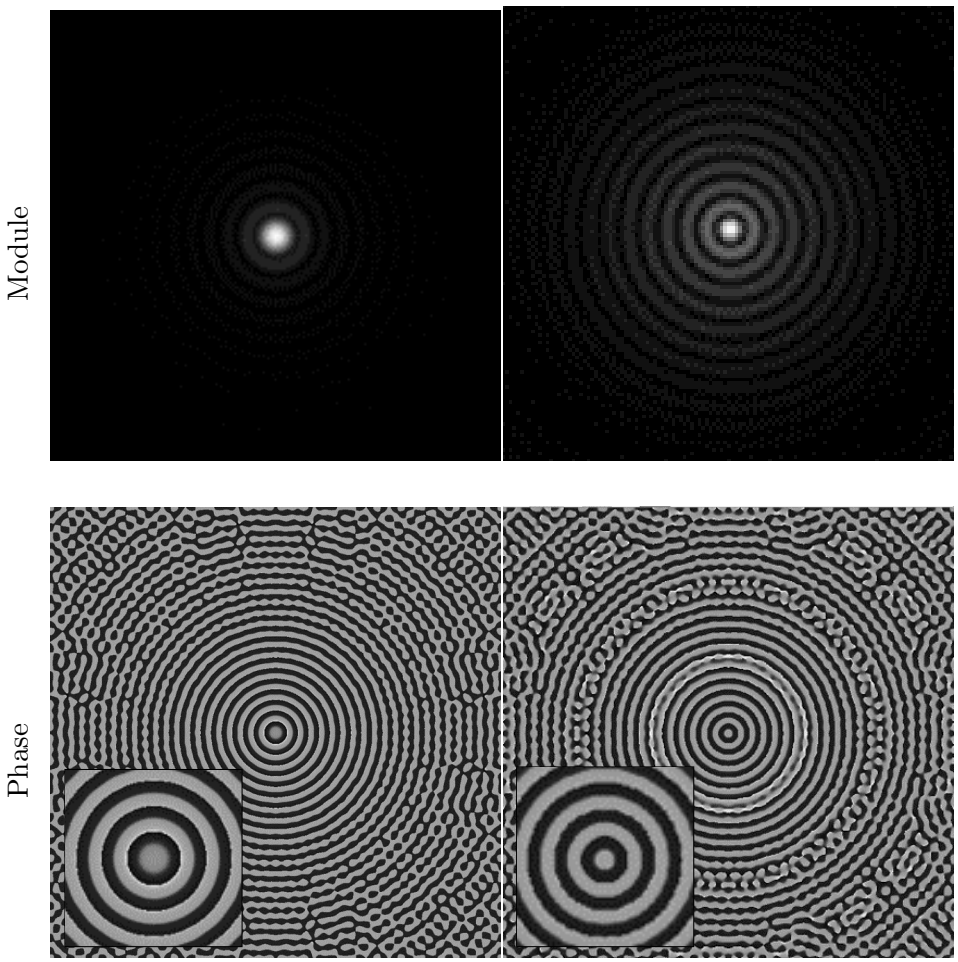

(a) 0 mrad **(b)** 18 mrad

Figure 9: Inner aperture - Insets show a magnification of the respective image centers.

Exercise 5 - Vortex beam

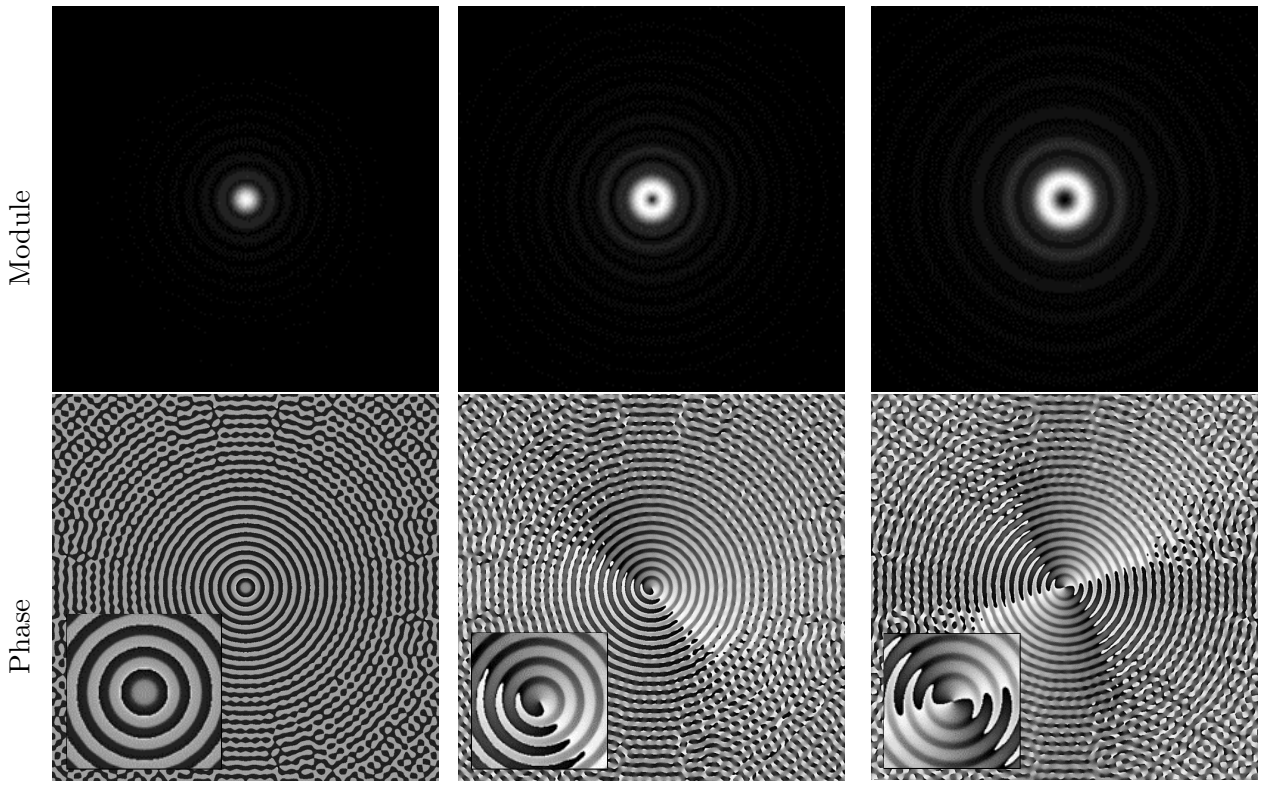

(a) m=0 **(b)** m=1 **(c)** m=2

Figure 10: Vortex beam - Insets show a magnification of the respective image centers.

Exercise 6 - Electron specimen interaction

- Phase object approximation

Generally, the electron wave function after the interaction with the specimen ($\psi_t(x)$) is the product of the incident wave function $\psi_{in}(x)$ and a transmission function $t(x)$.

$$\psi_t(x) = t(x)\psi_{in}(x) \tag{6}$$

A pure phase object only modifies the phase of the incident wave. The incident wave function in CTEM is approximately a plane wave ($\psi_{in} = 1$). Thus, the phase object is described by the transmission function $t(x)$.

$$\psi_{po}(x) = t(x)\psi_{in}(x) = e^{i\sigma v_z(x)}\psi_{in}(x) = e^{i\sigma v_z(x)} \tag{7}$$

The modulus of this wave function $\left|e^{i\sigma v_z(x)}\right| = 1$ Therefore, the image intensity shows nothing but computational noise, but the structure can be seen in the phase image. The effects are illustrated in figures 11a and 11b respectively.

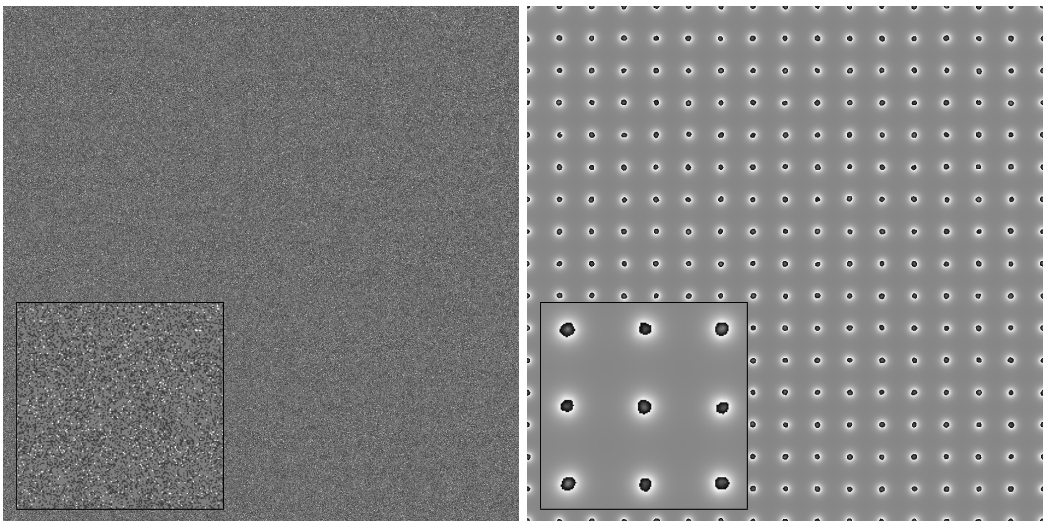

(a) Intensity **(b)** Phase

Figure 11: Phase object approximation

- Weak phase object approximation

In the weak phase object (WPO) approximation the specimen is assumed to be very thin and composed mainly of light atoms. The primary effect of the specimen is to produce a spatially varying phase shift in the electron wave function as it passes through the specimen [Kirkland, 2010]. Mathematically, the weak phase object is described by the low order terms of the power series expansion of the phase object:

$$\psi_{wpo}(x) \approx e^{i\sigma v_z(x)} \approx 1 + i\sigma v_z(x) + ... \tag{8}$$

The modulus of ψ_{wpo} is no longer just one. Hence, the structure now also appears in the intensity image, as shown in Figure 12.

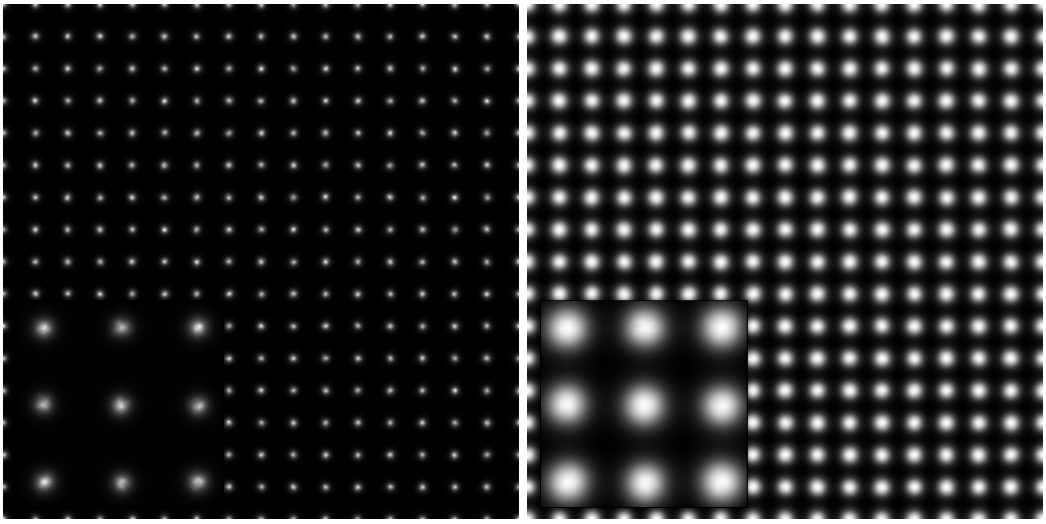

(a) Intensity **(b)** Phase

Figure 12: Weak phase object approximation

- Multislice approximation

In the standard multislice formulation, the specimen potential is divided into many slices perpendicular to the electron beam. Each slice has to be thin enough to be considered a weak phase object, which

modifies only the phase of the incident wave. The potential between two consecutive slices is considered to be zero and the propagation of the electron wave within the slice is approximated by the Fresnel propagator. The electron wave at any depth z can be calculated by repeated application of the last process, which is mathematically described by:

$$\psi_{MS} = P \otimes (e^{i\sigma v_z} \psi_n) \tag{9}$$

where P is the Fresnel propagator [Lobato, 2014]. This propagation of the wave function gives rise to interference, as shown in Figure 13.

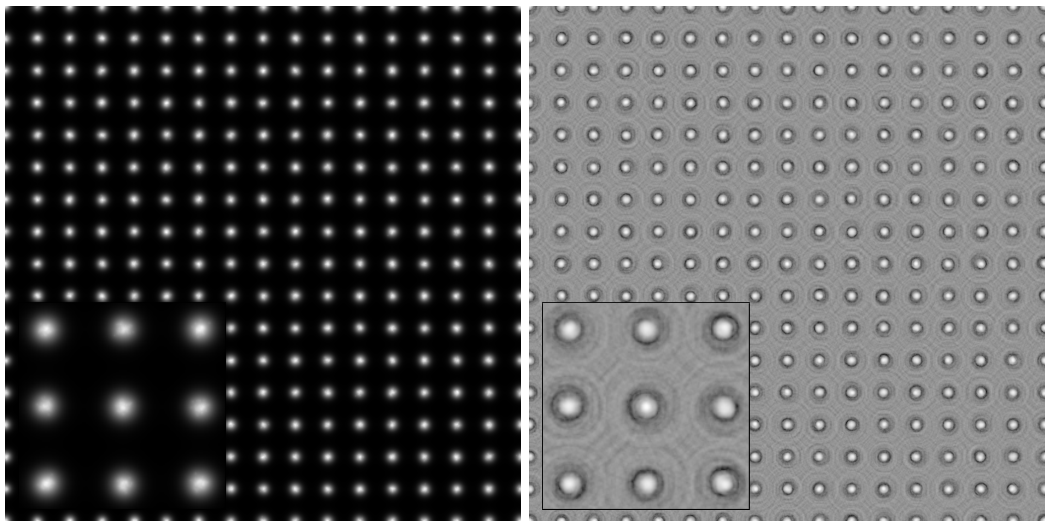

(a) Weak phase object solution **(b)** Multislice solution

Figure 13: Comparison of intensities (log-scale)

Exercise 7 - Electron phonon interaction

Phonons cause small deviations of the atoms positions (vibrations). Neglecting these deviations, results in Figure 14a. The interference is strongly pronounced because all atoms are exactly stacked over another within the columns. Introducing a random atomic position offset causes a blurring as seen in Figure 14b. Due to the high velocity of the probing electrons, it is save to assume that an electron wave would "see" one (frozen) phonon configuration. Averaging over ever more phonon configurations creates increasingly smooth images and more realistic simulations (figures 14b to 14d).

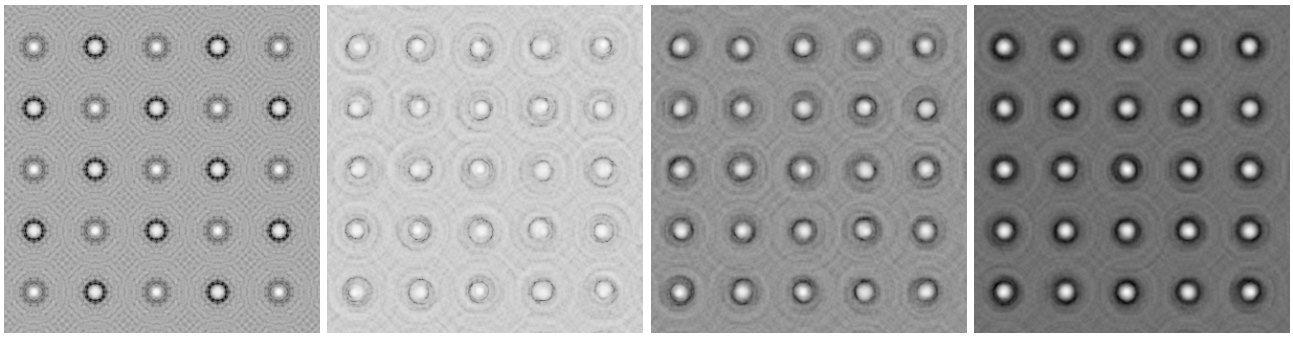

(a) Still atom approximation

(b) Frozen phonon approximation (1 Phonon)

(c) Frozen phonon approximation (5 Phonons)

(d) Frozen phonon approximation (20 Phonons)

Figure 14: Comparison of electron phonon interaction approximations (log-scale)

Exercise 8 - Adding vacuum

What is shown in Figure 15a is the so-called wrap-around error. Because the calculations use Fourier transforms, periodic boundaries are required. For an infinite crystal this condition is automatically fulfilled. However, for nanocrystals this is not the case. An atom at the edge of the image is wrapped around the boundary if you do not compensate by adding vacuum around the nanocrystal. In Figure 15a this effect is clearly visible at the lower and right hand side edges of the image. This wrap-around effect still occurs in Figure 15b, but it only affects regions of vacuum now. Therefore, the effect does not introduce artefacts in the simulations.

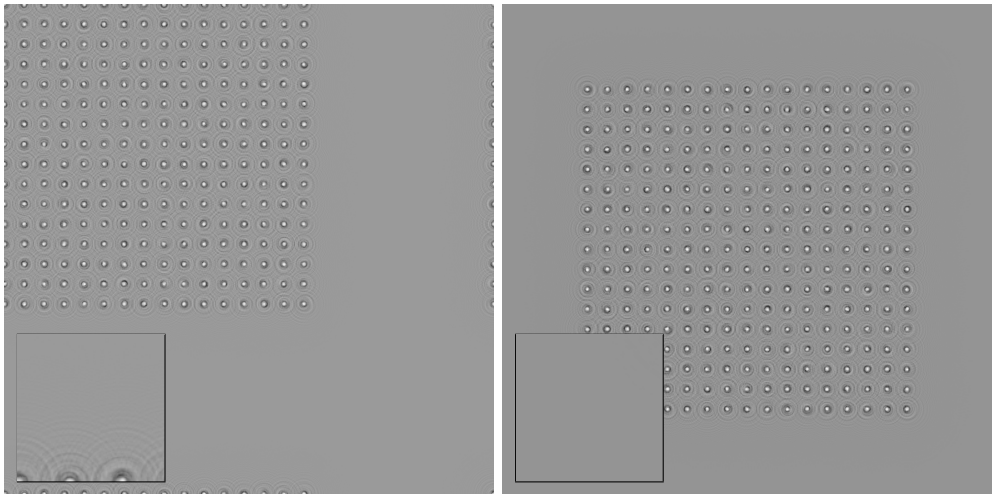

(a) Added vacuum (log-scale) **(b)** Recentered nanocrystal (log-scale)

Figure 15: Demonstration of wrap-around error - The insets show magnifications of the lower left corners respectively.

Exercise 9 - Rotation

A rotation of 45° of the Pt crystal in (001) orientation around the (100) axis would intuitively result in a change of the zone orientation to (110). However, the rotation does not result in the structure repetition one would want. Instead, Figure 16b is actually a simulation of a nanocrystal with varying thickness and subject to wrap-around errors. Adding vacuum avoids the wrap-around errors as seen in Figure 16c.

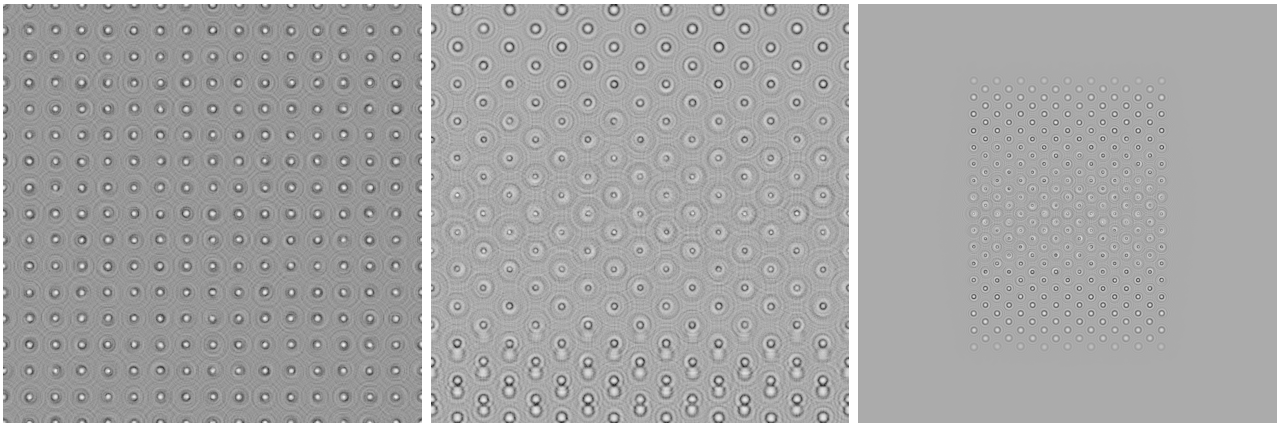

(a) Pt crystal (100), no rotation (log-scale) **(b)** Pt crystal (100), rotated 45° (log-scale) **(c)** Pt nanocrystal (100), rotated 45°, vacuum added (log-scale)

Figure 16: Rotation of crystals

Exercise 10 - Simulate crystal by thickness

What can be observed in this exercise is the first half period of the channelling oscillation (increase and decrease in intensity). Note that for running the *by thickness* option only makes sense if there is periodicity along the beam direction. Furthermore, *whole specimen* is a bit faster than *by thickness*, because extra memory is required to store the intermediate slice solutions.

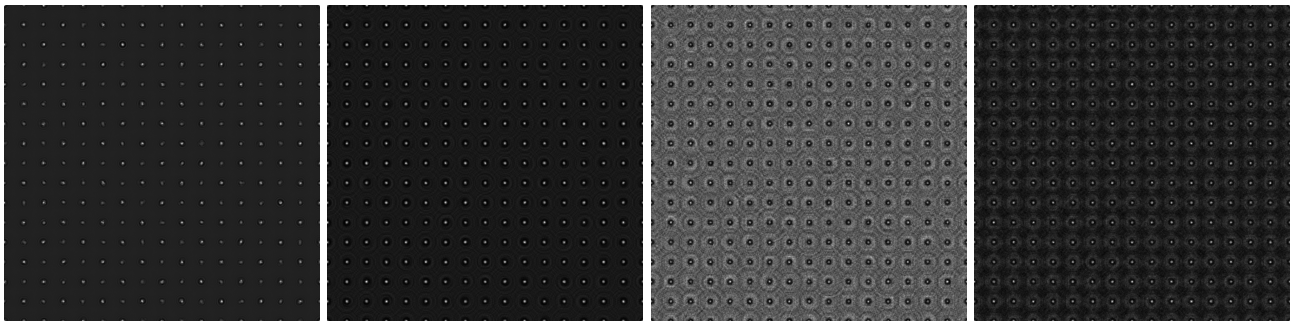

(a) Thickness: 4.078 Å **(b)** Thickness: 36.702 Å **(c)** Thickness: 61.170 Å **(d)** Thickness: 101.950 Å

Figure 17: Crystal simulation by thickness

Exercise 11 - Defocus

The zero reference of the defocus was changed in this exercise. Usually, the reference is set to the last atom (Figure 18c), but for experimental data, this point is not exactly known.

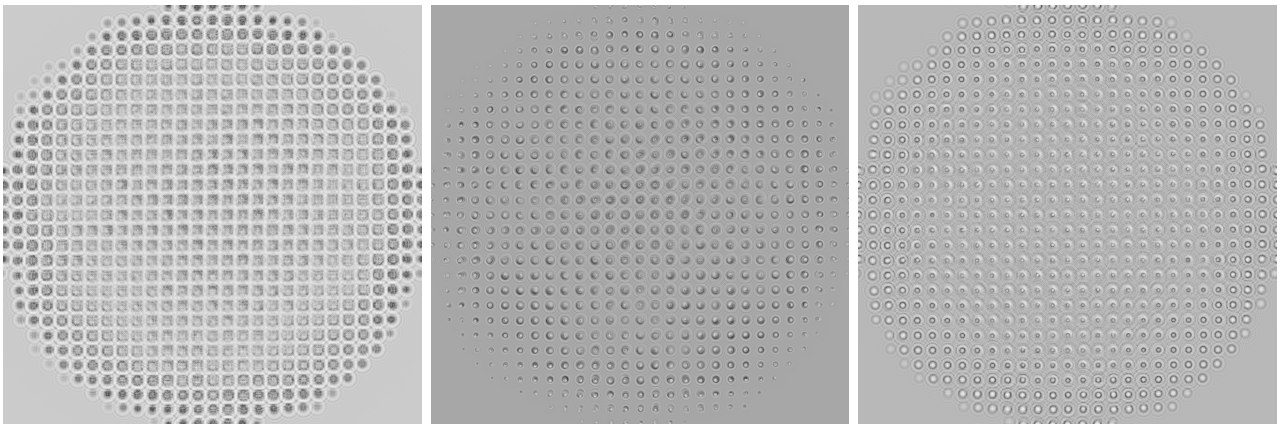

(a) Zero defocus at first atom **(b)** Zero defocus at the middle of the specimen **(c)** Zero defocus at the last atom

Figure 18: Defocus (log-scale)

Exercise 12 - Potential slicing

The multislice approximation is only correct within the limit of a very small slice of thickness. The relatively small difference between $dz = 2\,\text{Å}$ in Figure 19a and the slicing by planes method in Figure 19c is due to the program detecting the planes automatically, which is $\approx 2.0375\,\text{Å}$ for Gold. For a nanoparticle there is no periodicity in the planes. So for a nanoparticle it is better to define the slice thickness to for example 2 Å. The *by planes* option works very well for a slab of crystal.

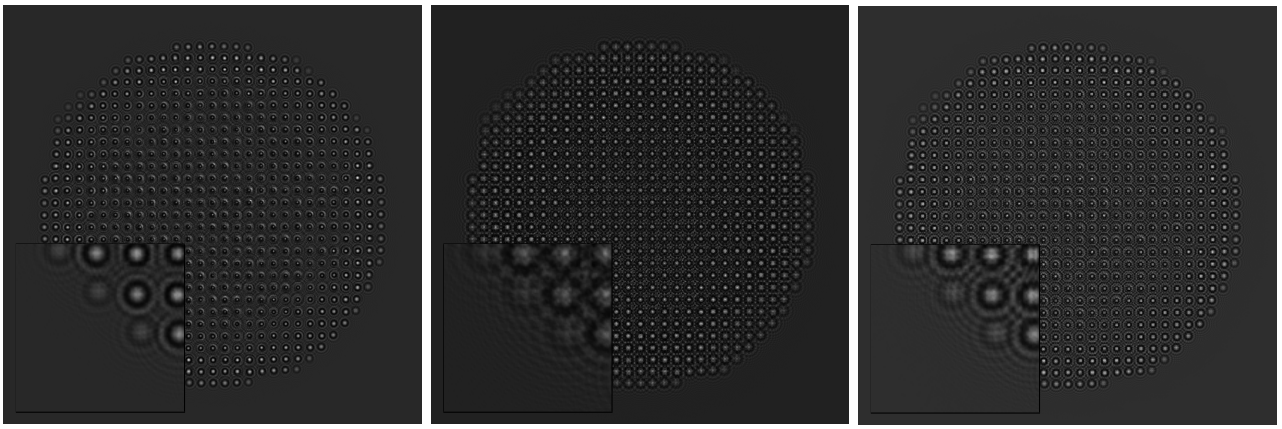

(a) $dz = 2\,\text{Å}$ **(b)** $dz = 20\,\text{Å}$ **(c)** Slicing by planes

Figure 19: Influence of potential slicing - The insets show magnifications of the lower left corners respectively.

Exercise 13 - Sampling

The sampling actually refers to the potential. It is essential to capture enough features of the potential to get correct results.

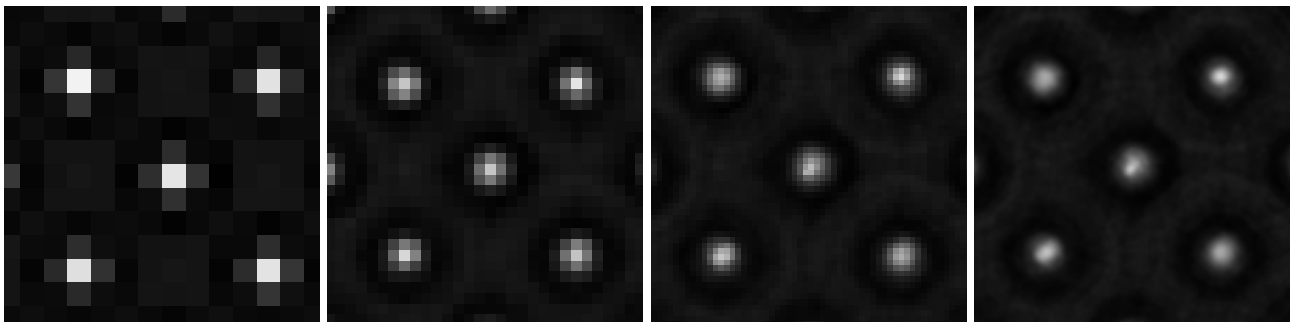

(a) Sampling: 128 x 128 **(b)** Sampling: 256 x 256 **(c)** Sampling: 512 x 512 **(d)** Sampling: 1024 x 1024

Figure 20: Influence of sampling

Exercise 14 - High resolution transmission electron microscopy

When looking at the images at different thicknesses, you notice a change in intensity, due to contrast reversal. As the wave propagates through the sample, the phase is being shifted further in each slice. This causes an intensity modulation along the thickness, according to the phase shift with a period of 2π.

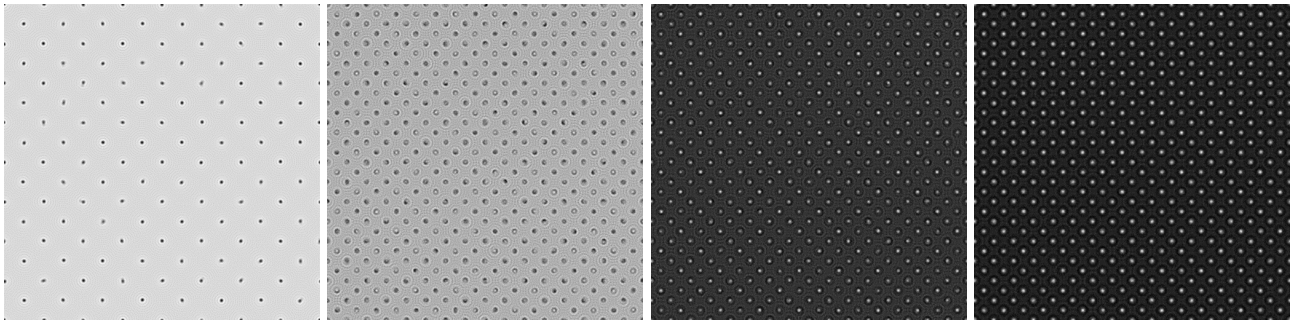

(a) Thickness: 0.0000 Å **(b)** Thickness: 16.2921 Å **(c)** Thickness: 32.5842 Å **(d)** Thickness: 54.3070 Å

Figure 21: Contrast reversal in HRTEM

Exercise 15 - Electron diffraction

a) Diffraction spots

You see some higher order reflections appear and disappear or vary in intensity with thickness

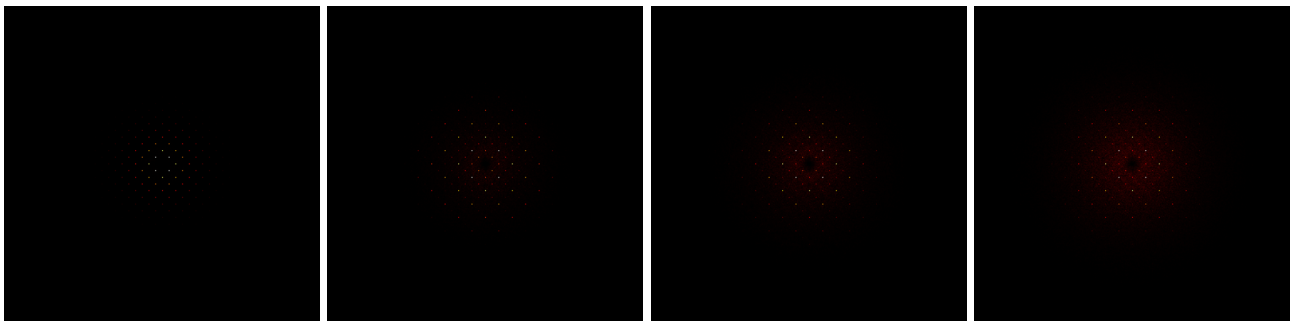

(a) Thickness: 0.0000 Å **(b)** Thickness: 16.2921 Å **(c)** Thickness: 32.5842 Å **(d)** Thickness: 54.3070 Å

Figure 22: Electron diffraction - diffraction spots

b) Kikuchi lines

With this Au sample also Kikuchi lines and high order Laue zones can be seen. Try to look at the image with jet colorscale or play with the scaling to enhance the contrast. In Figure 23, we used a power scaling with power 0.25.

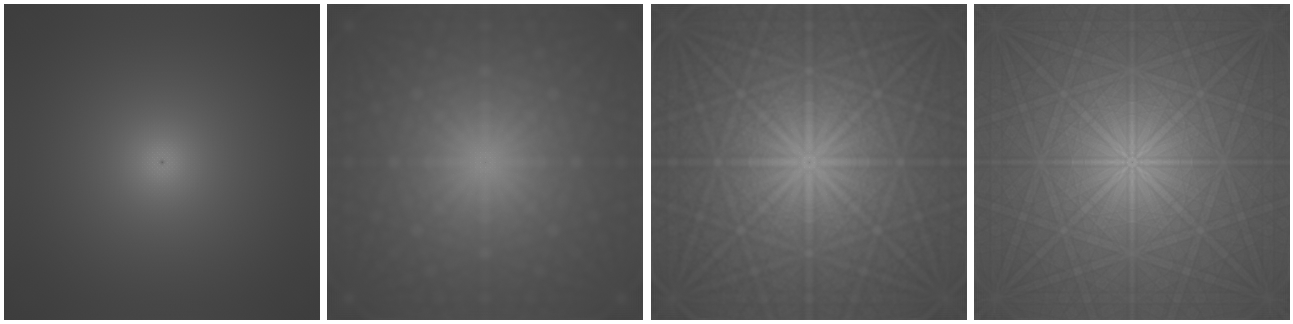

(a) Thickness: 4.078 Å **(b)** Thickness: 36.702 Å **(c)** Thickness: 61.170 Å **(d)** Thickness: 101.950 Å

Figure 23: Electron diffraction - Kikuchi lines

Exercise 16 - Scanning transmission electron microscopy

By increasing the amount of sampling points per area, more details become visible (Figures 24a and 24b). Detectors 1 and 2 effectively represent dark field (DF) and bright field (BF) detectors respectively (Figures 24c and 24d).

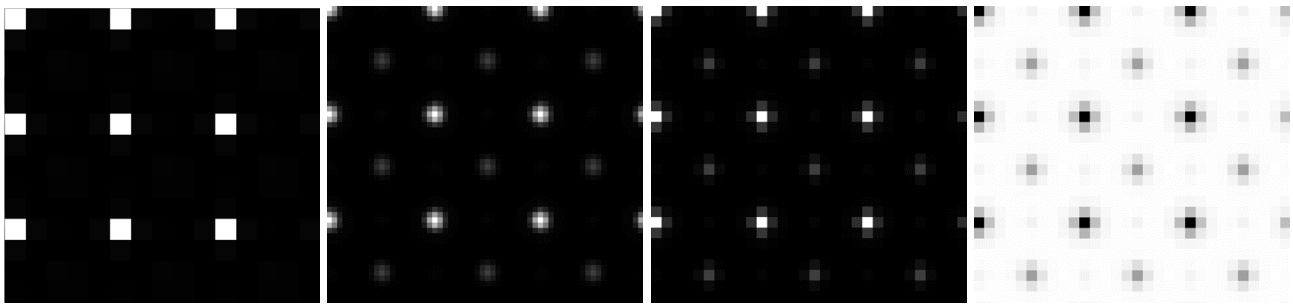

(a) 5 scan points **(b)** 20 scan points **(c)** 10 scan points, detector 1 (40-100 mrad) **(d)** 10 scan points, detector 2 (0-20 mrad)

Figure 24: Scanning transmission electron microscopy (STEM)

Exercise 17 - Energy filtered transmission electron microscopy

EFTEM allows the selective imaging of particular atoms, based on their specific inner shell ionisation energies (inelastic scattering) as shown in Figure 25. The donut shape of the imaged atoms makes sense physically but is usually not observed in experiments due to practical resolution limits.
Different channelling approximations used for these simulations are summarised in Figure 26. The most accurate is the double channelling approximation. After the inelastic scattering event occurs, the multislice method is applied for the rest of the specimen in the same manner. This is relatively slow, but accurate and should be used if computation time is not a concern. In the single channelling approximation, essentially the rest of the specimen is ignored after the inelastic event, saving computation time. The mixed channelling approximation is a compromise between the other two approximations by treating the section after the inelastic event as a single phase object. A detailed comparison of the performances and a more detailed description of these methods can be in found in [Lobato et al., 2016] and [Verbeeck et al., 2009].

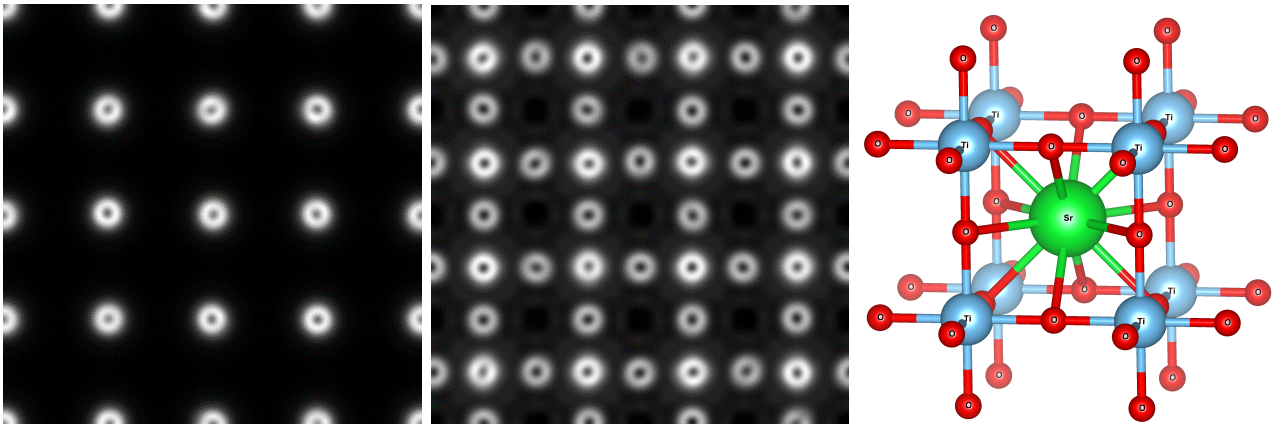

(a) Sr, energy edge 1940 **(b)** O, energy edge 532 **(c)** Perovskite structure $SrTiO_3$

Figure 25: EFTEM images simulations

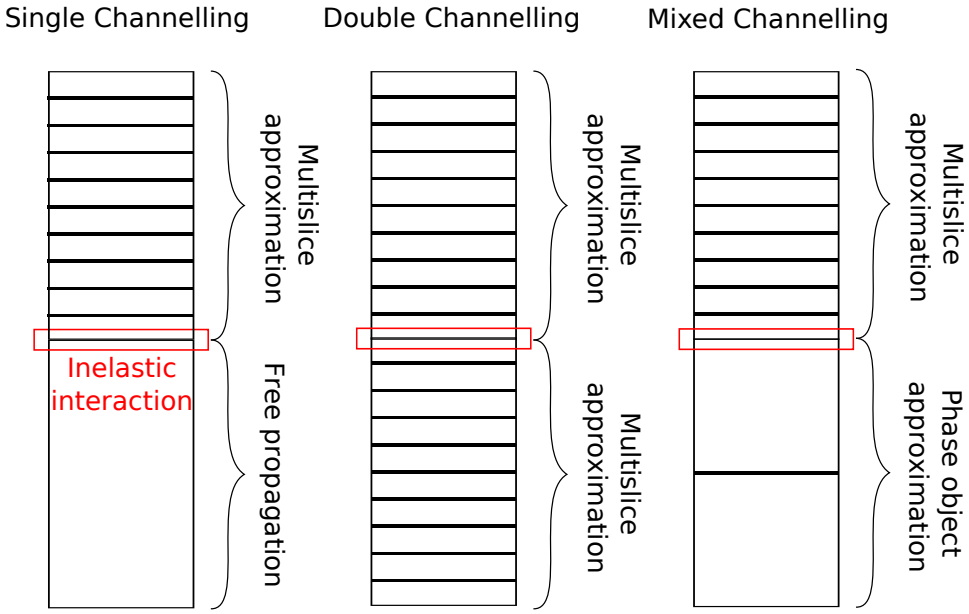

Figure 26: Channelling approximations for EFTEM

References

[Kirkland, 2010] Kirkland, E. J. (2010). *Advanced Computing in Electron Microscopy*. Springer New York Dordrecht Heidelberg London.

[Lobato et al., 2016] Lobato, I., Van Aert, S., and Verbeeck, J. (2016). Progress and new advances in simulating electron microscopy datasets using MULTEM. *Ultramicroscopy*, 168:17–27.

[Lobato, 2014] Lobato, I. P. (2014). *Accurate modeling of high angle electron scattering*. PhD thesis, University of Antwerp.

[Verbeeck et al., 2009] Verbeeck, J., Schattschneider, P., and Rosenauer, A. (2009). Image simulation of high resolution energy filtered tem images. *Ultramicroscopy*, 109(4):350 – 360.